ADVANCED FUNCTIONAL MATERIALS
www.afm-journal.de

Alleviation of Aging-Related Hallmarks in a Mouse Model of Progeria via a Nanoparticle-Based Artificial Transcription Factor

Hongwon Kim, Junyeop Kim, Euiyeon Lee, Brandon Conklin, Yannan Hou, Sumin Kim, Yerim Hwang, Ki-Bum Lee, and Jongpil Kim**

The increasing demand for precise and safe modulation of cellular-rejuvenation and reprogramming has driven the development of innovative nanotechnologies capable of achieving unprecedented control over cell fate and function. Among these, biomimetic nanoparticles stand out due to their enhanced biocompatibility, improved targeting capabilities, prolonged circulation time, and multifunctionality. These attributes position them as promising tools for advancing drug delivery, personalized medicine, and targeted therapies for various diseases. In this study, a novel nanoparticle-based artificial transcription factor developed, termed Oct4-nanoscript, specifically designed to emulate the function of the *Oct4* gene. This results support that the Oct4-nanoscript exhibits high-affinity DNA binding, efficient nuclear localization, and robust activation of Oct4 target genes. Furthermore, partial reprogramming induced by Oct4-nanoscript significantly reduced DNA damage and restored key epigenetic marks, hallmarks of cellular aging. In a Hutchinson-Gilford Progeria Syndrome (HGPS) mouse model, the Oct4-nanoscript effectively rescued age-related pathological features and extended lifespan. This non-viral, stable, and highly specific biomimetic nanoparticle platform for emulating Oct4 gene function presents a promising therapeutic strategy for age-related diseases, including HGPS. These findings advance the field of regenerative medicine, offering a foundation for developing innovative therapies targeting complex biological challenges.

1. Introduction

Biomimetic nanoparticles, which are carefully designed to replicate both the structure and function of natural cellular components, have emerged as a highly promising area of investigation in the field of biomedical research.[1] These engineered nanoparticles hold significant potential, particularly in advancing targeted drug delivery systems and the enhancement of the efficacy of gene therapy approaches.[2] Particularly, recent studies have increasingly highlighted the capacity of biomimetic nanoparticles to overcome physiological barriers, engage in considerably specific interactions with cellular and molecular targets, and deliver therapeutic payloads with a level of precision previously unattainable.[3] Their unique design and tunability allow for better investigation in complex biological microenvironments.

For example, nanozymes, a class of bio-nanomaterials engineered to mimic the catalytic activity of natural enzymes, are being explored as potential anti-aging therapeutics.[4] These nanozymes involve the modulation of reactive oxygen species levels, thereby mitigating oxidative stress, a key factor implicated in the aging process and various age-related pathologies.[5] Furthermore, extracellular vesicle-like biomimetic nanoparticles (EBPs) have received considerable attention as a versatile platform for targeted cancer therapy.[6] EBPs showed a combination of desirable characteristics, including low immunogenicity, which minimizes the risk of adverse immune responses, an extended circulatory half-life, allowing for prolonged therapeutic action, and enhanced targeting efficiency, which facilitates the precise delivery of therapeutic agents to cancerous tissues.[6,7] In our previous studies, we developed a nanoparticle-based artificial transcription factor platform called *NanoScript*, a synthetic biomimetic nanosystem engineered to replicate the multidomain structure and functionality of endogenous transcription factor proteins.[8] NanoScript-based activators, for example, have been designed to incorporate histone acetyltransferase molecules, enabling efficient chromatin remodeling and activation of chondrogenesis in mesenchymal stem cells (MSC).[9] Moreover, we generated a NanoScript-based

H. Kim, J. Kim, S. Kim, Y. Hwang, J. Kim
Laboratory of Stem Cells & Cell Reprogramming
Department of Chemistry
Dongguk University
Pildong-ro 1-gil 30, Jung-gu, Seoul 04620, Republic of Korea
E-mail: jpkim153@dongguk.edu
H. Kim, E. Lee, B. Conklin, Y. Hou, K.-B. Lee
Department of Chemistry and Chemical Biology
Rutgers
The State University of New Jersey
Piscataway, NJ 08854, USA
E-mail: kblee@rutgers.edu
The ORCID identification number(s) for the author(s) of this article can be found under https://doi.org/10.1002/adfm.202425944

DOI: 10.1002/adfm.202425944

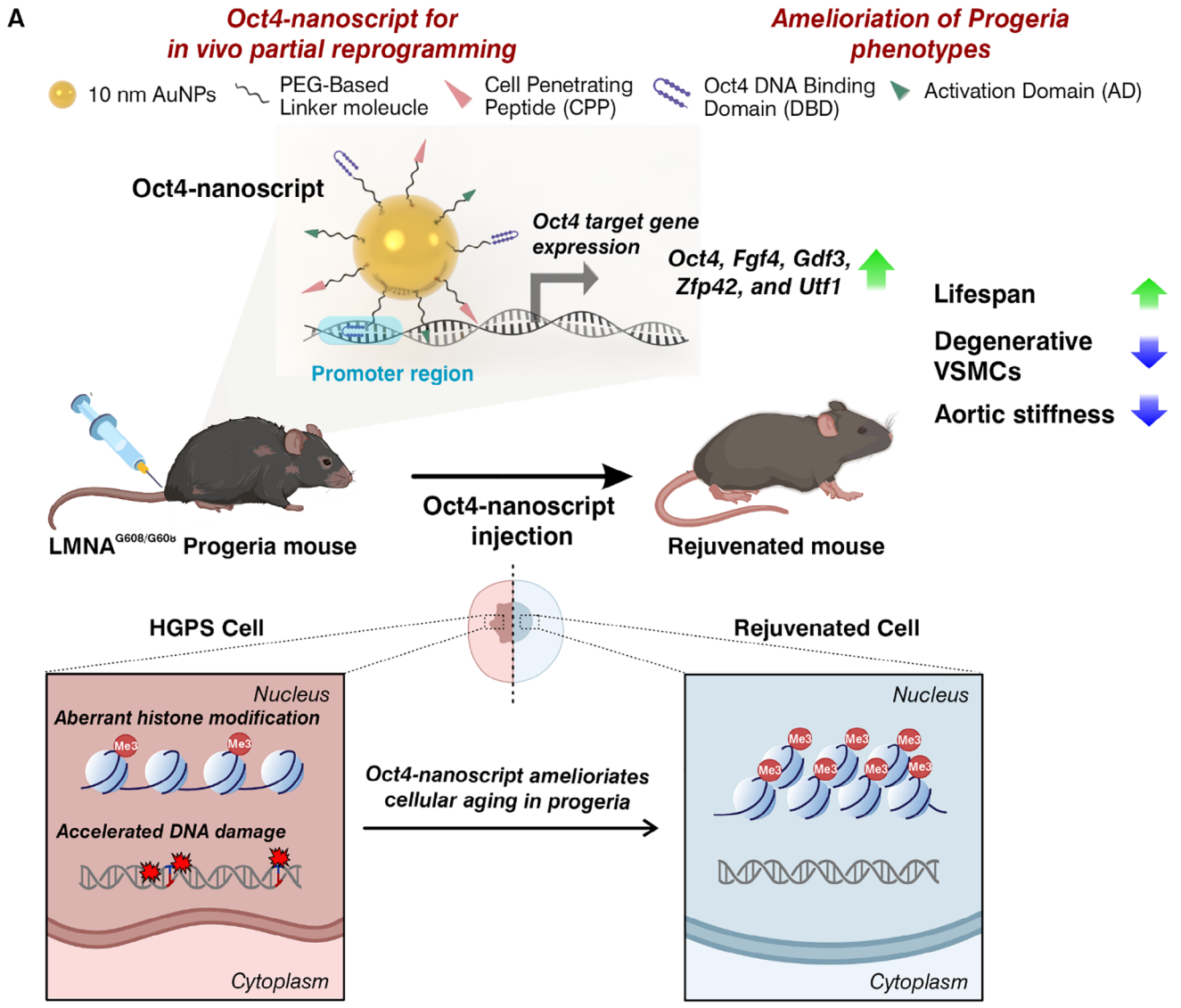

Figure 1. Schematic of the Oct4-nanoscript for ameliorating aging-associated hallmarks in a progeria mouse model. A) By assembling individual synthetic TF components, including the Oct4 DNA-binding domain (DBD), activation domain (AD), and cell-penetrating peptide (CPP), onto a single 10 nm gold nanoparticle, we engineered Oct4-nanoscript, a biomimetic construct designed to replicate the functional attributes of the endogenous Oct4 transcription factor. Activation of Oct4 target genes by Oct4-nanoscript ameliorates aging-associated phenotypes in LMNA$^{G608G/G608G}$ mice. Oct4-nanoscript was administered via tail-vein injection, reading to the restoration of cellular functions and the mitigation of progeria-associated pathological features.

myogenic transcription factor that successfully promotes the differentiation of adipose-derived MSCs into mature myocytes by precisely targeting key myogenic regulatory genes.[10] Similarly, NanoScript-based repressors, such as those targeting Sox9, have shown potent and specific gene silencing capabilities, effectively repressing Sox9 expression.[11] Taken together, these studies clearly indicate that the NanoScript platform can address key limitations of traditional gene regulation and cell therapy approaches, including the challenge of precise transgene expression control, dependence on viral delivery systems with their inherent risks, and potential off-target effects.

In particular, biomimetic NanoScripts can offer particularly unique advantages for cellular reprogramming and rejuvenation therapies within the field of regenerative medicine. Notably, the forced expression of four transcription factors, Oct4, Sox2, Klf4, and Myc (collectively known as OSKM or Yamanaka factors), can reprogram somatic cells to an induced pluripotent state, similar to embryonic stem cells. Importantly, transient expression of OSKM factors has demonstrated the ability to reverse age-associated cellular phenotypes.[13] This includes reducing DNA damage, restoring the normal nuclear envelope structure, alleviating cellular senescence, and correcting aberrant histone modifications, as observed in models of progeria.[14] More importantly, we have shown that endogenous Oct4 activation, particularly through CRISPR/dCas9-mediated transcriptional activation, is sufficient to induce partial cellular reprogramming and rejuvenation, effectively ameliorating age-related phenotypes.[15] Thus, these findings highlight the potential of biomimetic

nanoparticles to mimic Oct4 function, potentially inducing rejuvenation and offering a novel approach to cellular reprogramming and age-related interventions.

To achieve this, we have developed a novel biomimetic nanoparticle-based platform, termed *Oct4-nanoscript*, specifically designed for rejuvenation reprogramming. This biomimetic Oct4 NanoScripts enables specific and transient activation of the endogenous Oct4 gene, potentially circumventing the risks associated with traditional reprogramming factors, such as those employing viral vectors or constitutive expression of multiple factors. We further demonstrated that partial reprogramming, induced by Oct4-nanoscript, effectively reduces DNA damage and restores youthful epigenetic marks, both of which are established hallmarks of cellular aging in a mouse model of Hutchinson-Gilford Progeria Syndrome (HGPS) (**Figure 1**). Thus, our study highlights the broader implications of biomimetic nanoparticles, such as the Oct4-nanoscript platform, for regenerative medicine and their potential applications in treating a wide range of age-related diseases. The Oct4-nanoscript platform, in particular, offers a highly promising strategy for the precise modulation of cellular fate and function. Its capacity for targeted and transient gene activation not only addresses key challenges in traditional methods but also opens new avenues for personalized regenerative medicine.

2. Results

2.1. Synthesis and Characterization of Oct4-Nanoscript: A Biomimetic Nanoparticle Platform for Oct4 Gene

The Oct4-nanoscript, a biomimetic nanoparticle-based artificial transcription factor engineered to emulate the function of the endogenous Oct4 gene, was synthesized by integrating five key functional components onto a gold nanoparticle (AuNP) core: 1) a hairpin polyamide for specific binding to the Oct4 promoter region; 2) an activation domain-mimicking peptide to recruit transcriptional machinery; 3) a cell-penetrating peptide (CPP) to facilitate cellular uptake and nuclear translocation; 4) polyethylene glycol (PEG) molecules to improve stability and act as a linker; and 5) the AuNP core itself, which serves as a scaffold for assembly.

For the preparation of biomimetic nanoparticles for the Oct4 gene, we synthesized the hairpin polyamide DBD based on the design of a sequence incorporating pyrrole (Py) and imidazole (Im) motifs, which selectively bind to A-T and G—C base pairs, respectively, enabling the precise targeting of specific gene sequences.[16] Based on solid-phase synthesis protocol,[17] we prepared a hairpin polyamide DBD specific to the Oct4 binding motif, termed Oct4-DBD, with the sequence PyPy-β-ImPyPy-γ-PyImPy-β-PyPy-β-Dp, where γ is γ-aminobutyric acid, β is β-alanine, and Dp is dimethylaminopropylamide, matching the consensus promoter sequence of Oct4 gene (**Figure 2A**). Surface plasmon resonance analysis demonstrated that Oct4-DBD exhibits a high binding affinity of 1.14×10^{-8} M for its target sequence (Figure 2B). Additionally, liquid chromatography-mass spectrometry analysis confirmed the molecular weight of Oct4-DBD as 1708.9 m z^{-1} (Figure S1A, Supporting Information).

For the activation domain component of Oct4-nanoscript, we designed peptide sequences known for their robust transactivation properties, which effectively induce transcriptional activity. Additionally, PEG molecules were incorporated to significantly enhance the solubility of the conjugated biomolecules and stabilize the nanoparticles within physiological environments. Specifically, thiol-terminated PEG molecules were employed to functionalize a mixed monolayer on the surface of the gold nanoparticles. This functionalization enhances the stability and biocompatibility of the nanoparticles while providing a versatile platform for the attachment of other functional components in the Oct4-nanoscript system. Subsequently, Oct4-DBD, AD, and a CPP were conjugated to thiol-terminated PEG molecules, followed by their assembly with 10 nm AuNPs to construct Oct4-nanoscript (Figure 2A,C). Dynamic light scattering and transmission electron microscopy revealed that the final Oct4-nanoscript construct possesses a hydrodynamic diameter of 56.9 ± 12.2 nm and a surface charge of 0.6 ± 0.3 mV (Figure 2D,E). Collectively, these findings provide compelling evidence for the successful assembly of a stable and functional biomimetic nanoparticle platform, termed Oct4-nanoscript, specifically engineered for the targeted modulation of Oct4 genes.

2.2. Intracellular Localization of Oct4-Nanoscript: Nuclear Accumulation

We first conducted a dose-dependent cell viability assay over 5 days to determine any cytotoxic effects of NanoScript on the fibroblasts. We found that concentrations up to 20 µg/mL of NanoScript treatment maintained high levels of cell viability, ranging from 90–97% (Figure 2F,G). These findings indicate that Oct4-nanoscript is biocompatible and does not exhibit any cytotoxic effects on mouse fibroblasts at concentrations up to 20 µg mL^{-1}, supporting its safety for cellular applications at this dosage.

All transcriptional activity occurs exclusively inside the nucleus; hence, an important criterion for Oct4-nanoscript to regulate gene expression is efficient cellular internalization and nuclear localization. To monitor intracellular localization, nanoscript combined with a FITC dye incubated in mouse fibroblasts. The overlap of fluorescein isothiocyanate (FITC) and 40, 6-diamidino-2-phenylindole (DAPI) in mouse fibroblasts treated with Oct4-nanoscript confirmed that Oct4-nanoscript was able to translocate within the nucleus after 24 h (Figure 2H; Figure S1B, Supporting Information). Remarkably, a significant increase in the number of FITC-expressing cells was observed in mouse fibroblasts treated with 20 µg mL^{-1} of Oct4-nanoscript (Figure 2I). Consistently, real-time live-cell imaging confirmed the initial intracellular distribution of nanoscript within 4 h post-treatment (Figure S1C, Supporting Information). Moreover, fluorescence imaging revealed a time-dependent increase in the intracellular localization of Oct4-nanoscript, with a notably higher number of FITC-tagged nanoscript particles observed at 48 h post-treatment compared to 4 or 12 h (Figure S1D, Supporting Information). Importantly, nuclear translocation of the nanoscript was more prominent at 24–48 h (Figure S1B,D, Supporting Information), whereas at earlier time points, the majority of the nanoscript remained in the cytoplasm. This suggests a gradual intracellular processing of the nanoscript leading to its nuclear localization over time. In addition, we observed no cytotoxicity of Oct4-nanoscript through co-staining FITC-tagged

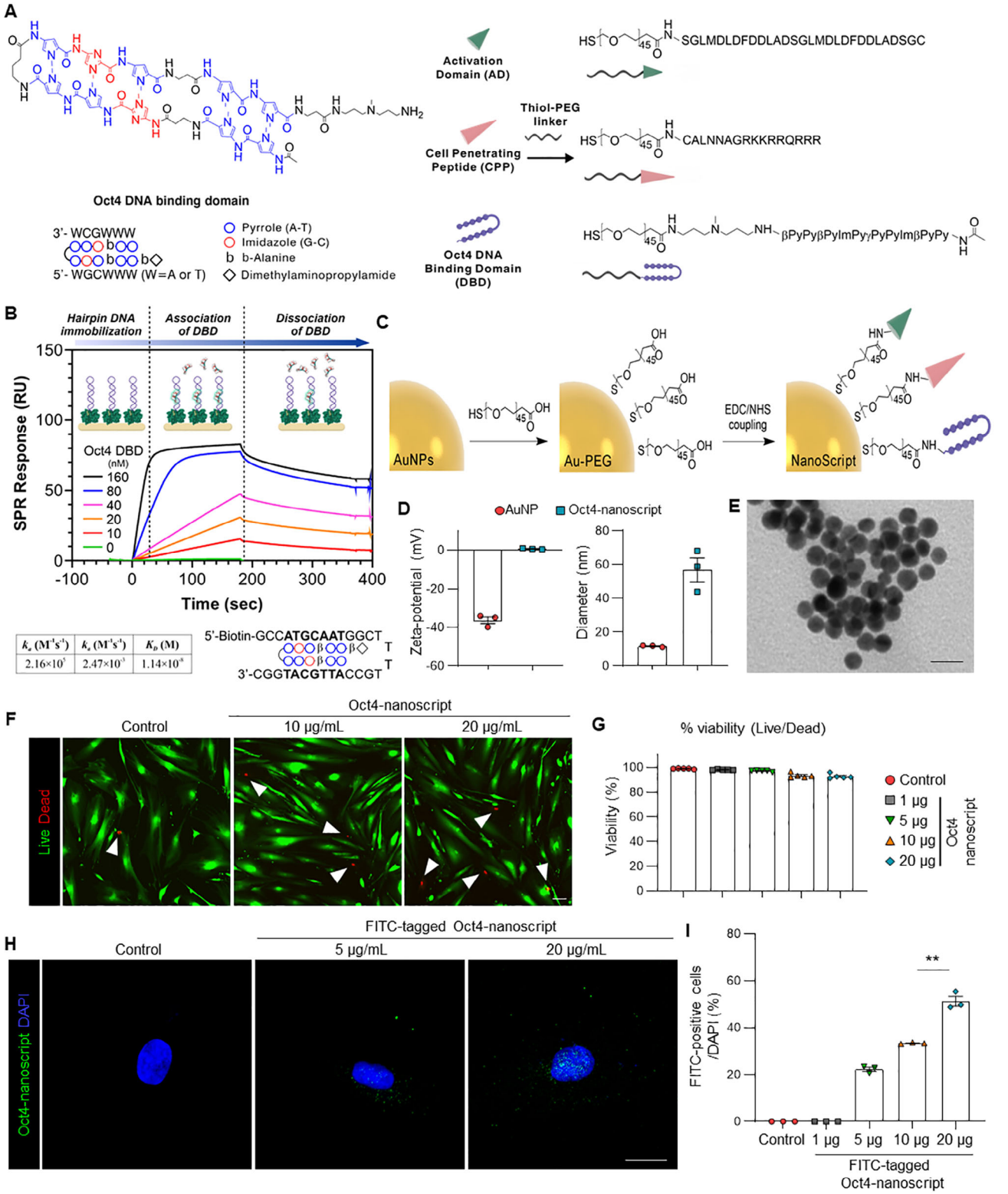

Figure 2. Preparation and Characterization of Oct4-nanoscript. A) Chemical structures of each biomolecule (Oct4-DBD, AD, CPP, and peptide linker). Each biomolecule was conjugated to the thiol-PEG-carboxy linker molecule. Oct4-DBD, with pyrrole (blue) and imidazole (red) motifs arranged in a specific sequence to complement the Oct4 response element. B) Surface plasmon resonance assay of specific binding affinities of varying polyamide Oct4-DBD concentrations with the complementary hairpin DNA. The Oct4 polyamide was designed in a specific sequence to complement the 5′-ATGCAAT-3′ Oct4 binding motif. The equilibrium constant (K_D), which is indicative of the binding affinity, was determined by the ratio of the dissociation constant (k_d) to the association constant (k_a). C) Illustration of synthesis of Oct4-nanoscript linked to NLS, AD, and Oct4-DBD on AuNP. D) Characterization

Oct4-nanoscript with H3K9me3, p16INK4A, and LaminA/C in the mouse fibroblasts (Figure S1E, Supporting Information). Furthermore, no differences were observed in the number of irregular nuclei 5 days after Oct4-nanoscript treatment (Figure S1F, Supporting Information). Overall, these data suggest that Oct4-nanoscript is adequately small to facilitate efficient nuclear entry and accumulation. This characteristic underscores its potential for effective intracellular delivery and precise nuclear targeting, making it a promising tool for cell reprogramming applications.

2.3. Evaluation of Oct4-Nanoscript-Induced Reprogramming in Mouse Fibroblasts

To evaluate whether Oct4-nanoscript can activate endogenous Oct4 target genes, we transduced fibroblasts with Oct4-nanoscript and first examined its ability to induce the activation of the endogenous *Oct4* gene (**Figure 3A**). Previous studies showed that the endogenous Oct4 binds to the DNA binding motifs located within promoter or enhancer regions of the *Oct4* gene (Figure S2A, Supporting Information).[18] Notably, the distal enhancer of *Oct4* contains a specific binding motif that recruits transcriptional factors such as Oct4 and Sox2.[19] Consistent with these results, we observed a significant upregulation ($p < 0.01$) of *Oct4* expression at five days post-treatment of mouse fibroblasts with Oct4-nanoscript (Figure 3B,C). In contrast, NanoScript constructs lacking any of these key components did not induce *Oct4* expression (Figure 3C), suggesting that the full complement of functional domains in Oct4-nanoscript is essential for its activity in activating Oct4 target gene expression.

We also found that *Oct4* expression was significantly elevated at 5 days following treatment with 5–20 μg mL^{-1} of Oct4-nanoscript compared to the untreated control (Figure 3D). However, activation of *Oct4* expression was not sustained, as no expression was observed after 15 days of Oct4-nanoscript treatment (Figure 3E; Figure S2B, Supporting Information). Consistent with these findings, we detected Oct4-positive cells and elevated Oct4 protein levels in fibroblasts 5 days post-treatment with 20 μg mL^{-1} of Oct4-nanoscript (Figure 3F–H), showing that Oct4-nanoscript can efficiently activate the expression of *Oct4* gene. The time points were selected based on the distinct times of transcriptional activation and subsequent cellular changes. *Oct4* mRNA expression peaked at day 2, reflecting early transcriptional activation, whereas protein expression and phenotypic changes required additional time to manifest.

Additionally, the expression of *Sox2*, which contains an Oct4 binding motif in its promoter region, was marginally elevated for the initial 5 days, whereas *Nestin, Klf4, and c-Myc* expression remained undetectable upon Oct4-nanoscript treatment (Figure S2C–E, Supporting Information). These results strongly suggest that the gene expression induced by Oct4-nanoscript is sufficient to activate downstream pluripotency-associated genes involved in partial reprogramming. Furthermore, the expression of Oct4 target genes, including *Fgf4*, *Gdf3*, *Zfp42*, and *Utf1*, which contain the Oct4 binding motif in their promoter regions, was significantly upregulated ($p < 0.01$) in fibroblasts treated with Oct4-nanoscript compared to the control (Figure S3A–C, Supporting Information). Taken together, these findings provide compelling evidence that Oct4-nanoscript functions effectively as an artificial transcription factor, mimicking endogenous Oct4 activity to activate downstream target genes and initiate the cascade of events leading to cellular reprogramming.

Moreover, we observed that Oct4-nanoscript increased the mRNA levels of genes associated with the mesenchymal-to-epithelial transition (MET), including *E-cadherin*, *Ssea1*, and *Cldn3*, while reducing the mRNA levels of epithelial-to-mesenchymal transition (EMT)-related genes, such as *N-cadherin*, *Zeb2*, and *Twist1* (Figure 3I). Notably, treatment of Oct4-nanoscript caused dramatic alterations in the expression levels of MET/EMT-related genes, similar to the lentiviral Oct4 expression (Figure 3I). Collectively, these findings provide compelling evidence that Oct4-nanoscript can promote cellular rejuvenation in skin fibroblasts. This effect appears to be mediated by the induction of MET, the concurrent suppression of epithelial-to-mesenchymal transition, and the functional emulation of the endogenous Oct4 transcription factor, collectively driving cellular de-differentiation.

2.4. Rejuvenation Reprogramming of Progeria Fibroblasts Using Oct4-Nanoscript

Next, to investigate Oct4-nanoscript's potential to induce rejuvenation reprogramming in aged fibroblasts, we treated fibroblasts from $LMNA^{G608G/G608G}$ progeria mice with Oct4-nanoscript. Previous studies showed that H3K9me3 and H4K20me3, key epigenetic marks involved in heterochromatin maintenance, have been shown to undergo aging-associated alterations in progeria models, reflecting age-related chromatin reorganization.[15,20] Notably, we observed that Oct4-nanoscript treatment increased H3K9me3 levels and decreased H4K20me3 levels in aged fibroblasts from these mice (**Figure 4A–C**; Figure S4A–C, Supporting Information). Given that DNA double-strand breaks are associated with cellular aging,[21] we assessed the level of phosphorylated histone gamma-H2AX, a marker of such breaks, 10 days after the treatment with varying concentrations of Oct4-nanoscript. Remarkably, phosphorylated histone gamma-H2AX was significantly reduced ($p < 0.01$) by the Oct4-nanoscript treated in $LMNA^{G608G/G608G}$ fibroblasts (Figure 4D,E). Moreover, the number of cells with phosphorylated histone gamma-H2AX was also significantly reduced ($p < 0.01$) as a result of NanoScript-mediated activation of Oct4 target gene expression (Figure 4F,G;

using a zetasizer confirmed the diameter and surface charge of NanoScript. Data represent mean±SEM. $n = 3$ per each sample. E) Transmission electron micrographs of Oct4-nanoscript. Scale bar = 20 nm. F) Representative images of Calcein AM- or EthD-1-positive cells in mouse fibroblasts treated with different concentrations of Oct4-nanoscript (ranging from 1–20 μg). White arrows indicate nonviable cells. Scale bar = 50 μm. G) Percentage viability of mouse fibroblasts treated with different concentrations of Oct4-nanoscript at 5 days. Data represent mean ± SEM. *One-way ANOVA-test*; $n = 5$ per group. H) Representative images of FITC-expressing cells in mouse fibroblasts treated with FITC-tagged Oct4-nanoscript. Scale bar = 20 μm. I) Quantification of FITC-expressing cells in mouse fibroblasts treated with different concentrations of FITC-tagged Oct4-nanoscript. Data represent mean ± SEM. *One-way ANOVA-test*, $^{**}P < 0.01$; $n = 3$ per group.

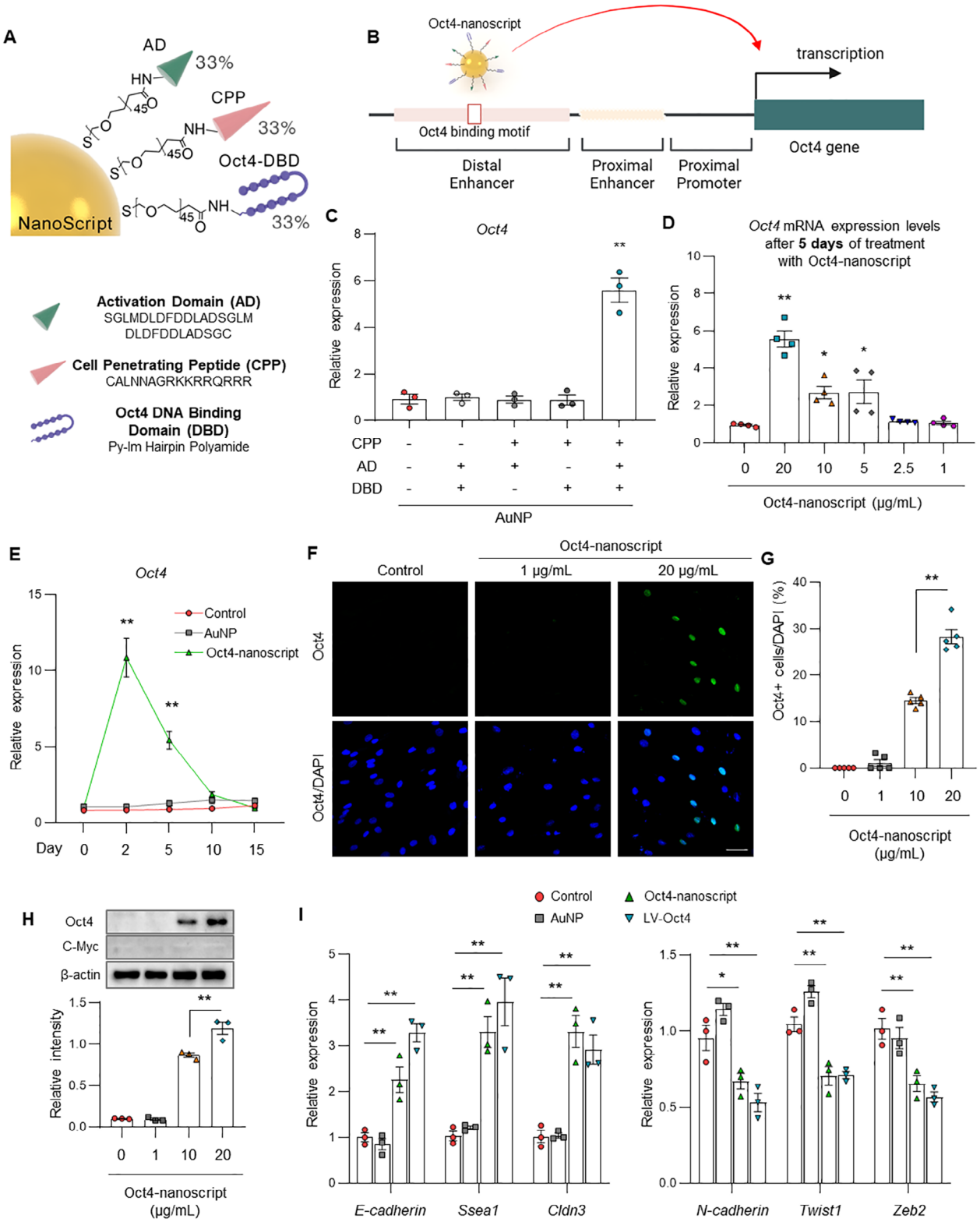

Figure 3. Functional activity of Oct4-nanoscript in fibroblasts. A) Illustration of the structure of Oct4-nanoscript linked to NLS, AD, and Oct4-DBD on AuNP. B) Schematic diagram of the mouse Oct4 distal enhancer, proximal enhancer, and proximal promoter. Oct4-nanoscript recognizes specific Oct4 binding motifs at the Oct4 distal enhancer. C) qRT-PCR analysis of *Oct4* expression in different component conditions for 5 days. Data represent mean ± SEM. *One-way ANOVA-test*, $^{**}P < 0.01$; $n = 3$ per group. D) *Oct4* mRNA expression levels after 5 days of treatment with Oct4-nanoscript at different concentrations. Data represent mean ± SEM. *One-way ANOVA-test*, $^{*}P < 0.05$, $^{**}P < 0.01$; $n = 4$ per group. E) qRT-PCR analysis of *Oct4* expression in

Figure S5A, Supporting Information). Furthermore, we demonstrate that the expression of p16INK4A, which is a well-known biomarker for cellular senescence,[22] is significantly reduced ($p < 0.01$) in $LMNA^{G608G/G608G}$ mutant fibroblasts treated with Oct4-nanoscript compared to untreated $LMNA^{G608G/G608G}$ mutant fibroblasts (Figure 4H–J; Figure S5B, Supporting Information). The phenotypic effect of Oct4-nanoscript on the nuclear morphology of $LMNA^{G608G/G608G}$ fibroblasts was measured using ImageJ-plugins analysis of the nucleus circularity and roundness parameter (Figure S5C,D, Supporting Information).[23] Consistently, the number of $LMNA^{G608G/G608G}$ mutant cells with abnormal nuclei decreased 10 days after the treatment of the Oct4-nanoscript (Figure 4K,L). These results showed that the NanoScript-mediated expression of the Oct4 target genes can efficiently ameliorate aging-related molecular phenotypes in $LMNA^{G608G/G608G}$ mutant fibroblasts in vitro.

2.5. In Vivo Therapeutic Effects of Oct4-Nanoscript in a Mouse Model of Progeria Syndrome

First, to confirm the in vivo delivery and nuclear localization of Oct4-nanoscript, we analyzed liver and kidney tissues 24 h after tail vein injection of FITC-labeled Oct4-nanoscript in $LMNA^{G608G/G608G}$ progeria mice. We observed that Oct4-nanoscript was localized in the nuclei of liver and kidney cells (Figure S6A, Supporting Information). Next, to assess the therapeutic efficacy of Oct4-nanoscript via inducing endogenous Oct4 gene expression, we evaluated Oct4 expression across various organs after systemic administration of Oct4-nanoscript in mice. Consistently, Oct4-nanoscript treatment significantly increased endogenous *Oct4* expression in the liver, aorta, kidney, and spleen compared with saline controls (**Figure 5A**). Endogenous *Oct4* expression peaked on day 3 post-injection and gradually declined by day 7 (Figure 5B). Notably, *Oct4* was selectively upregulated, while *Sox2*, *Klf4*, and *c-Myc* showed no significant changes. Furthermore, *Nanog*, a marker of full reprogramming, was not induced, indicating that Oct4-nanoscript specifically targets endogenous *Oct4* without activating other pluripotency genes (Figure 5C). Additionally, Oct4-nanoscript treatment in wild-type mice showed no significant differences in distance traveled or average velocity in the open field test, indicating no adverse effects on mobility or activity levels (Figure S6B, Supporting Information). Also, there were no significant changes in the expression of cancer-related genes *Afp* and *CD44*, suggesting that Oct4-nanoscript does not induce tumorigenic effects in vivo (Figure S6C, Supporting Information). Furthermore, to evaluate the long-term safety of Oct4-nanoscript, wild-type mice were monitored for 5 months following treatment. qPCR analyses confirmed that the expression levels of *Nanog* and cancer-related genes, including *Afp* and *CD44*, were not persistently upregulated beyond the transient Oct4 activation (Figure S6D, Supporting Information). Overall, these results demonstrate that Oct4-nanoscript can selectively induce partial expression of the endogenous Oct4 gene in multiple organs while maintaining a favorable safety profile, as it does not cause altered mobility or tumorigenesis.

To investigate the therapeutic potential of Oct4-nanoscript in reversing aging phenotypes, we administered Oct4-nanoscript to 4-month-old $LMNA^{G608G/G608G}$ progeria mice once weekly for 15 weeks. Remarkably, mice treated with Oct4-nanoscript showed significant improvements in physical appearance, including a reduction in gray hair and improved spinal curvature, compared to saline-treated controls (Figure 5D). Survival rates were markedly improved in the Oct4-nanoscript treated group, with both the median and maximal lifespan significantly extended compared to the saline-treated group (Figure 5E). Furthermore, body weight analysis revealed that Oct4-nanoscript treated progeria mice maintained significantly higher body weights compared to saline-treated progeria mice (Figure 5F). In addition to these systemic improvements, α-SMA-positive smooth muscle cells were significantly increased in the aorta of Oct4-nanoscript-treated progeria mice compared to saline-treated controls (Figure 5G,H). Moreover, adventitia thickness was reduced, and the adventitia/media ratio was improved in the Oct4-nanoscript treated group compared to the saline treted group (Figure S6E, Supporting Information). Histological analysis of the liver, spleen, and kidney revealed structural restoration in Oct4-nanoscript-treated progeria mice (Figure 5I). Quantitative analysis showed that hepatocyte density and the percentage of binucleated hepatocytes in the liver, the area of germinal centers and red pulp in the spleen, and diameters of renal tubule and tubular lumen size in the kidney were markedly improved in the Oct4-nanoscript treated group compared to saline-treated gruop (Figure 5J; Figure S6F, Supporting Information). These findings suggest that Oct4-nanoscript treatment promotes tissue integrity and regeneration across multiple organs in $LMNA^{G/G}$ progeria mice. Also, Oct4-nanoscript treatment significantly reduced the expression of *IL-6*, *Btg2*, and *Mmp13*, which are upregulated with aging, in progeria mice (Figure 5K). This result indicates that Oct4-nanoscript reduced age-related inflammation, aberrant cell proliferation, and extracellular matrix remodeling. Additionally, muscle strength was significantly improved in the Oct4-nanoscript-treated group compared to saline controls (Figure 5L). Overall, these results demonstrate that Oct4-nanoscript treatment effectively reverses age-related phenotypes in progeria mice by restoring tissue structure, reducing inflammation, and promoting functional recovery, highlighting its potential as a therapeutic strategy for age-related conditions.

3. Discussion

In short, our study introduces a novel therapeutic strategy using a biomimetic nanoparticle platform designed to function as a

mouse fibroblasts treated with 20 µg of Oct4-nanoscript over a period of 0 to 15 days. Data represent mean ± SEM. *One-way ANOVA-test*, $^{**}P < 0.01$; $n = 3$ per group. F) Representative images of Oct4-positive cells in mouse fibroblasts treated with Oct4-nanoscript. Scale bar = 50 µm. G) Quantification of Oct4-positive cells in mouse fibroblasts treated with Oct4-nanoscript at 1 week. Data represent mean ± SEM. *One-way ANOVA-test*, $^{**}P < 0.01$; $n = 5$ per group. H) Western blot analysis of Oct4 in mouse fibroblasts treated with different concentrations. Data represent mean ± SEM. *One-way ANOVA-test*, $^{**}P < 0.01$; $n = 3$ per group. I) qRT-PCR analysis of MET markers (*E-cadherin*, Ssea1, *Cldn3*) and EMT markers (*N-cadherin*, *Twist1*, *Zeb2*) under different conditions for 7 days. Data represent mean ± SEM. *One-way ANOVA-test*, $^{*}P < 0.05$, $^{**}P < 0.01$; $n = 3$ per group.

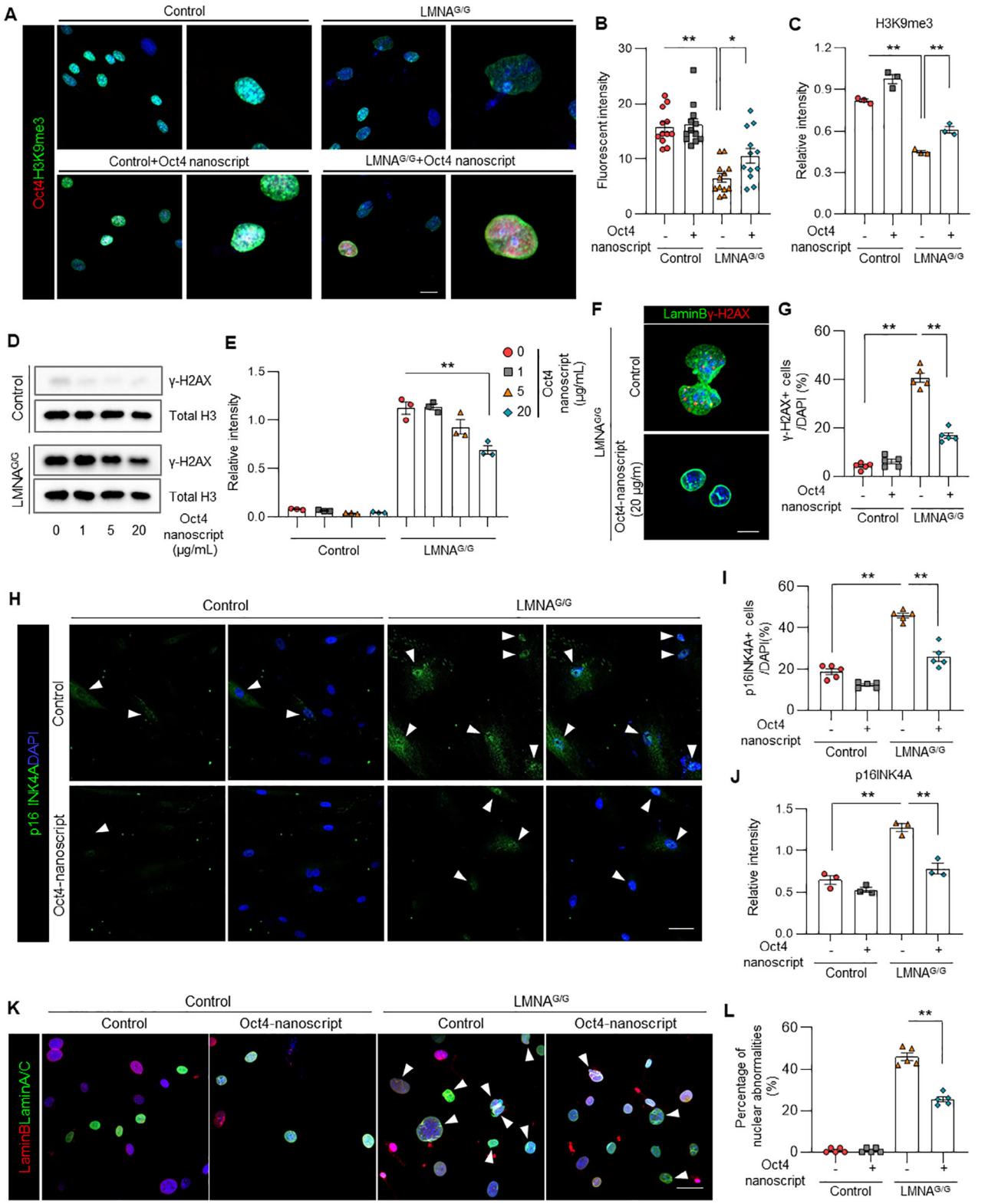

Figure 4. Amelioration of aging-associated hallmarks in LMNA G608G cells via Oct4-nanoscript. A) Immunofluorescence for Oct4+ and H3K9me3+ cells in control and LMNA$^{G/G}$ fibroblasts with or without Oct4-nanoscript. Scale bar = 20 μm. B) Quantification of the fluorescence intensity of H3K9me3 in nuclei using a single confocal section. Data represent mean ± SEM. *Two-way ANOVA-test*, $^{*}P < 0.05$, $^{**}P < 0.01$; $n = 12$ from three samples per group. C) The relative intensity of H3K9me3 levels in control and LMNA$^{G/G}$ fibroblasts treated with Oct4-nanoscript. Data represent mean ± SEM. *Two-way ANOVA-test*, $^{**}P < 0.01$; $n = 3$ per group. D,E) Western blot analysis of γ-H2AX and total histone H3 in control and LMNA$^{G/G}$ fibroblasts treated with

synthetic transcription factor, effectively emulating the functional properties of endogenous Oct4. Specifically, we demonstrated that Oct4-nanoscript exhibits high binding affinity to target DNA sequences associated with Oct4-regulated genes, achieves efficient nuclear localization, and drives robust transcriptional activation. Notably, Oct4-nanoscript significantly upregulated the expression of Oct4 and its downstream target genes, enabling partial reprogramming without triggering the expression of oncogenic markers such as c-Myc. In a Hutchinson-Gilford Progeria Syndrome (HGPS) model, Oct4-nanoscript exhibited a significant rejuvenating effect, underscoring its therapeutic potential in addressing age-related diseases, including HGPS. These findings also highlight the promise of Oct4-nanoscript as an innovative tool for safe and effective gene regulation and regenerative medicine.

The Oct4-nanoscript platform, based on a biomimetic nanoparticle, offers several advantages for inducing rejuvenation reprogramming and potentially treating age-related diseases. *First*, the nanoparticle's design enhances delivery and targeting capabilities, likely improving cellular uptake and biocompatibility. This targeted delivery could lead to more effective rejuvenation outcomes while avoiding genomic alterations, a significant advantage over traditional gene therapy methods. *Second*, by focusing on a single factor, Oct4, the Oct4-nanoscript approach may reduce the oncogenic risks associated with multi-factor reprogramming approaches, including potentially harmful factors like c-Myc. *Third*, the nanoparticle-based system allows for precise temporal and spatial control over Oct4 activation, facilitating transient partial reprogramming, which helps maintain cellular identity while still achieving rejuvenation effects. *Furthermore*, the platform's favorable safety profile is noteworthy, as evidenced by the lack of tumorigenic effects or altered mobility in wild-type mice. The transient nature of Oct4 expression induced by Oct4-nanoscript further mitigates potential risks associated with prolonged pluripotency factor expression, such as teratoma formation.

Previous studies have shown that Oct4 alone can initiate transcriptional resetting, potentially through interactions with endogenous pluripotency factors.[24] Consistently, our findings suggest that Oct4-nanoscript-mediated partial reprogramming is primarily driven by the activation of key Oct4 target genes, rather than the induction of the full pluripotency network. While *Sox2* expression exhibited a marginal increase in the early phase, *Klf4* and *c-Myc* remained undetectable, indicating that other yamanaka factors were not involved in the partial reprogramming. Instead, the significant upregulation of *Fgf4*, *Gdf3*, *Zfp42*, and *Utf1*, all of which contain Oct4-binding motifs, suggests that Oct4-nanoscript functions as an artificial transcription factor, selectively triggering transcriptional programs associated with reprogramming. This mechanism may facilitate epigenetic remodeling and transcriptomic shifts toward a partially reprogrammed state, without requiring the activation of the complete pluripotency-inducing network. Consistent with our result,[15] these findings highlight the potential of Oct4-centric strategies for controlled cellular reprogramming, providing an alternative approach distinct from conventional OSKM-based methods.

One of the most intriguing findings of our study is the broad impact of Oct4-nanoscript across multiple organ systems. The observed improvements in the liver, spleen, kidney, and cardiovascular system suggest that this therapy could have wide-ranging applications in treating systemic age-related decline. This multi-organ effect is particularly valuable in addressing complex, age-related conditions that simultaneously affect multiple body systems, offering a potential for holistic rejuvenation.

Although Oct4-nanoscript has been reported to ameliorate aging-related phenotypes in HGPS mice, the underlying molecular mechanisms—particularly those involved in restoring H3K9me3-positive heterochromatin loss—remain incompletely understood. We propose several potential mechanisms by which Oct4-nanoscript contributes to the restoration of these repressive histone marks in progeroid cells. First, Oct4-nanoscript may facilitate the recruitment of histone methyltransferases like SUV39H1 (for H3K9 trimethylation) and SUV420H1/2 (for H4K20 trimethylation), both critical for heterochromatin formation. Second, as a pioneer transcription factor, Oct4-nanoscript may initiate chromatin remodeling by accessing compacted regions, enabling heterochromatin re-establishment. Given the reduction of H3K9me3 and H4K20me3 in HGPS cells, further studies are needed to clarify how Oct4-nanoscript restores these marks. A focused analysis of these epigenetic changes could elucidate Oct4-nanoscript's chromatin-modulating effects and its therapeutic potential for laminopathy-associated premature aging.

In the future, exploring the efficacy of Oct4-nanoscript in addressing other age-related diseases and conditions beyond Hutchinson-Gilford Progeria Syndrome (HGPS) could significantly expand its therapeutic applications. Additionally, further refinement of the Oct4-nanoscript design—focusing on enhancing its targeting efficiency, cellular uptake, and gene activation potency—would further optimize its performance and therapeutic potential.

In conclusion, our study highlights the transformative potential of synthetic biology, exemplified by the innovative Oct4-nanoscript platform. These findings underscore its promise for clinical applications in regenerative medicine and the development of novel therapeutic strategies to address complex biological challenges and age-related disorders.

different concentrations. Data represent mean ± SEM. *Two-way ANOVA-test*, $^{**}P < 0.01$; $n = 3$ per group. F) Representative images of Lamin B- and γ-H2AX-positive cells in $LMNA^{G/G}$ fibroblasts with or without Oct4-nanoscript. Scale bar = 10 µm. G) Quantification of γ-H2AX-positive cells in each condition at 2 weeks. Data represent mean ± SEM. *Two-way ANOVA-test*, $^{**}P < 0.01$; $n = 5$ per group H) Immunofluorescence for p16 INK4A+ cells in control and $LMNA^{G/G}$ fibroblasts treated with Oct4-nanoscript. Scale bar = 50 µm. The white arrows indicate the p16 INK4A-expressing cells. I) Quantification of the p16 INK4A-positive cells in control and $LMNA^{G/G}$ fibroblasts treated with Oct4-nanoscript. Data represent mean ± SEM. *Two-way ANOVA-test*, $^{**}P < 0.01$; $n = 5$ per group. J) The relative intensity of p16 INK4A levels in control and $LMNA^{G/G}$ fibroblasts treated with Oct4-nanoscript. Data represent mean ± SEM. *Two-way ANOVA-test*, $^{**}P < 0.01$; $n = 3$ per group. K) Immunofluorescence for Lamin B+ and Lamin A/C+ cells in control and $LMNA^{G/G}$ fibroblasts with or without Oct4-nanoscript. Scale bar = 50 µm. L) Quantification of the nuclear abnormalities in control and $LMNA^{G/G}$ fibroblasts with or without Oct4-nanoscript. Data represent mean ± SEM. *Two-way ANOVA-test*, $^{**}P < 0.01$; $n = 5$ per group.

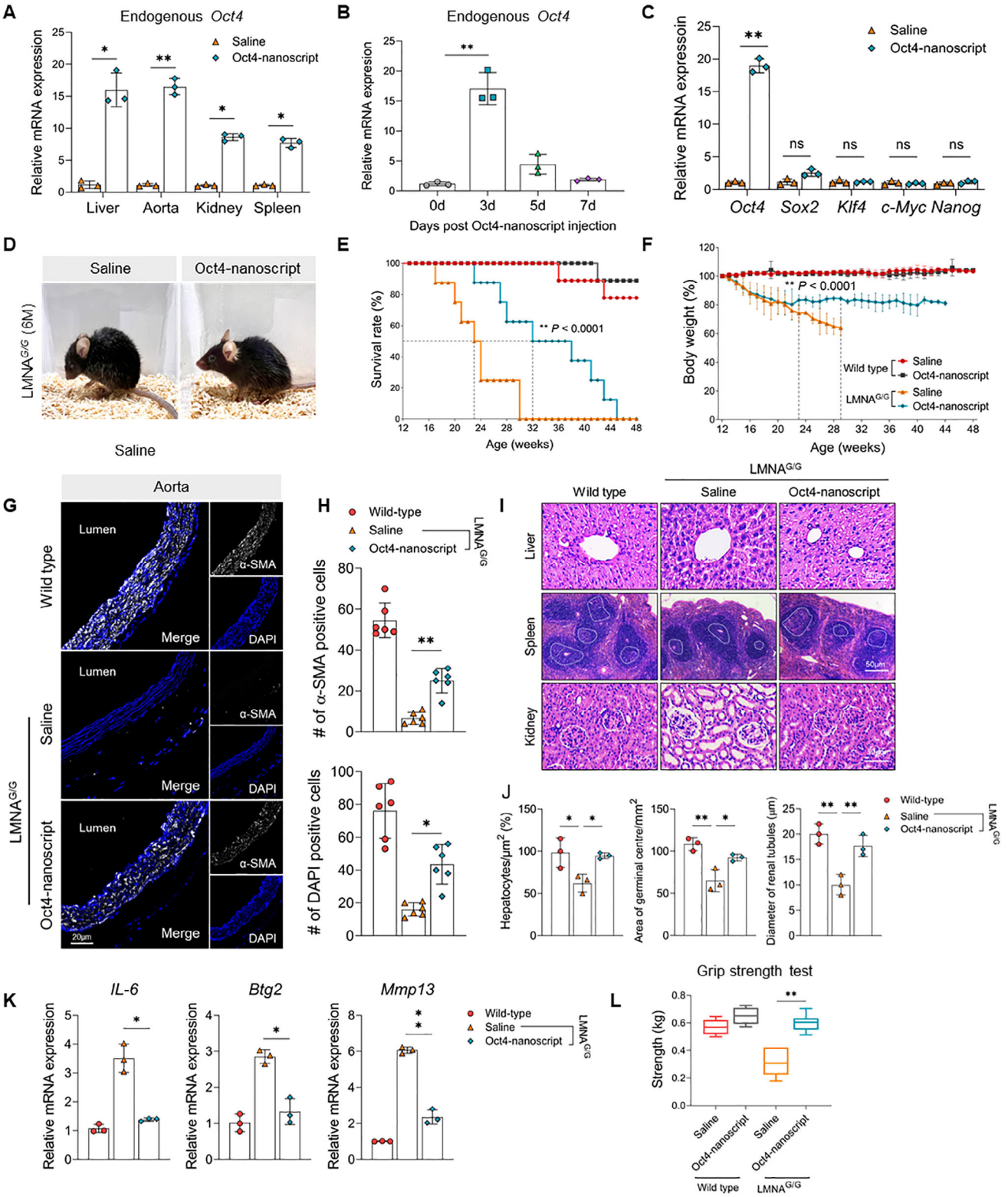

Figure 5. Amelioration of aging-associated hallmark in progeria mouse via Oct4-nanoscript. A) Relative mRNA expression levels of endogenous *Oct4* in the liver, aorta, kidney, and spleen after Oct4-nanoscript or saline treatment. Data represent mean±SEM. *Two-tailed Student's t-test*, $*P < 0.05$, $**P < 0.01$; $n = 3$ per each group. (B) Relative mRNA expression levels of *Oct4*, *Sox2*, *Klf4*, *c-Myc*, and *Nanog* in liver tissues from Oct4-nanoscript and saline-treated groups. Data represent mean±SEM. *Two-tailed Student's t-test*, $**P < 0.01$; $n = 3$ per each group. (C) Relative mRNA expression levels of endogenous *Oct4* at 0, 3, 5, and 7 days post-Oct4-nanoscript injection. Data represent mean ± SEM. *One-way ANOVA-test*, $**P < 0.01$; $n = 3$ per group. (D) Representative images of LMNA$^{G/G}$ progeria mice treated with saline (left) or Oct4-nanoscript (right). (E) Survival rates of LMNA$^{G/G}$ progeria mice

4. Experimental Section

Preparation of Oct4-DNA Binding Domain: The synthesis of the polyamide was performed by modifying a previously reported protocol.[25] The Oct4 polyamide with sequence AcPyPyβImPyPyγPyImPyβPyPyβDp (γ is γ-aminobutyric acid, β is β-alanine, and Dp is dimethylaminopropylamide), was synthesized on 40 mg of Fmoc-β-Ala-Wang resin (ca. 0.517 mmol g^{-1}, 100–200 mesh, aapptec) by using Fmoc chemistry. The following synthetic procedure was performed: i) The Wang resin was swollen with DMF for 30 min, prior to coupling. ii) The N-terminal Fmoc group was removed using 20% piperidine in DMF for 4 min (2 times), followed by washing with DMF. iii) Each of the corresponding carboxylic acids was activated with 1H-Benzotriazolium, 1-[bis(dimethylamino)methylene]-5chloro-hexafluorophosphate (1-),3-oxide (HCTU) (88 mg) and diisopropylethylamine (DIEA) and transferred to a reaction vessel for coupling with stirring by Argon gas bubbling. After the completion of the synthesis by the last acetyl capping (acetic anhydride and DIPEA in DMF) on the reaction vessel, the resin was washed with DMF and DCM, and dried in a desiccator at room temperature in vacuo. The Kaiser test was used to monitor the completion of the coupling steps. The dried resin was cleaved with 0.4 ml of 3,3′-diamino-N-methyldipropylamine for 3 h at 45 °C. Then the reaction mixture was filtered, triturated from CH_2Cl_2-Et_2O. This yielded a white-yellow crude powder. UPLC-Q-TOF/MS analysis was performed using the Waters Acquity UPLC H-Class system. The chromatographic separation of samples was carried out on a Waters Acquity UPLC BEH C18 column (2.1 × 50 mm; 1.7 µm). A linear gradient elution of solvent consisting of (A) H_2O and (B) acetonitrile, both containing 0.1% formic acid aqueous solution, were performed as follows: 100–100% A (0.0–0.5 min), 100–65% A (0.50–7.75 min), 65-5% A (7.75–8.50 min), 5–95% A (8.50–8.51 min), 95%–95% A (8.51–10.00 min) at a flow rate of 0.4 mL min^{-1}. The injection volume was 10 µl. MS analysis was performed in positive electrospray ionization (ESI) modes with the mass ranging from 300 to 2500 Da using Waters Xevo G2-XS QTof mass spectrometer. ESI-TOF-MS (positive) *m/z* calculated for $C_{80}H_{101}N_{29}O_{15}^{+}$ $[M+H]^+$ 1709.88; found 1709.84.

SPR Analysis: SPR experiments were performed on a Biacore 8K+ instrument (Cytiva, Sweden). A biotinylated hairpin DNA (5′-biotin-GCC**ATGCAAT**GGCTTTTGCC**ATTGCAT**GGC-3′) was purchased from Integrated DNA Technologies (Coralville, IA). A streptavidin-functionalized SA sensor chip was purchased from Cytiva. The biotinylated DNA was immobilized on the sensor chip to obtain the desired immobilization level (≈700 RU rise). The SPR assays were carried out using HBS-EP buffer (0.01 M HEPES, pH 7.4, 0.15 M NaCl, 3 mM EDTA, 0.05% surfactant P20) with 0.1% DMSO at 25 °C. The sample solution of Oct4 DBD with various concentrations were prepared in the buffer with 0.1% DMSO and injected at a flow rate of 20 µl min^{-1}. To calculate association rates (k_a), dissociation rates (k_d), and dissociation constants (K_D), data processing was performed with 1:1 binding model with mass transfer using Biacore Insight Evaluation 5.0.18.

Characterization of Oct4-nanoscript: *ζ-potential*: Zeta potential measurements were obtained on a Malvern Zetasizer Nano series using Malvern Disposable folded capillary cells (DTS1070).

Characterization of Oct4-nanoscript—Transmission Electron Microscopy (TEM): TEM grids were prepared by adding 10 µL of 1mg mL^{-1} of the sample onto the grid and were allowed to dry overnight in a vacuum desiccator. TEM images of the system were acquired using a JEOL transmission electron microscope (JEM 1010; JEOL, Japan) with an accelerating voltage of 80kV.

Preparation of Oct4-nanoscript: The Oct4-nanoscript construct was synthesized as per our previous publication.[8a] In short, amine-terminated biomolecules were conjugated to a linker molecule, SH-PEG-COOH [thiol-PEG-carboxy2 kDA (Creative PEGWorks, PBL-8073)]. The PEG linker was dissolved in dimethylformamide (DMF) to create a 50 mM solution, similarly a 1 M of N-hydroxysuccinimide (NHS) (Acros Organics) in DMF and 500 mM of 1-ethyl-3-(3-(dimethylamino)propyl) carbodiimide) (EDC) (Sigma) in DMF and minimal amounts of water to promote solubility were created. To activate the carboxyl group, EDC and NHS were added sequentially to the 50 mM PEG linker such that their final concertation was 50 mM and were shaken at room temperature overnight. Next, 10 mM solutions of the various domains (i.e., the DBD, AD, and NLS [TAT]) were added to the activated PEG linker such that the final concertation of the PEGylated domains was 10 mM. Finally, a mixture containing 30% SH-PEG-AD, 30% SH-PEG-DBD, 30% SH-PEG-NLS, and 10% SH-PEG-COOH by volume was added to 1 mL of 10 nm gold nanoparticle solution (TED-Pella: 15703–20) slowly over ice to create Oct4-nanoscript. The construct was purified by washing with deionized water through a 10000 MCWO filter (Millipore) to remove unreacted molecules and adjust the final volume. The dye-labeled Oct4-nanoscript was designed by conjugating fluorescein to SH-PEG-NH_2 and replacing 2% of the SH-PEG-COOH in the aforementioned solution with SH-PEG-Dye.

Animal Experiments: All procedures involving animals used in experiments were performed in accordance with institutional guidelines for animal use and received ethical approval from the Institutional Animal Care and Use Committee at Dongguk University. Control wild-type C57BL/6 male mice (Korea Research Institute of Bioscience & Biotechnology) and the HGPS mice carrying the G608G laminA/C mutation (The Jackson Laboratory, stock number 101 667) were used. All the mice were maintained on a 12 h/12 h light/dark cycle (light on and off at 9:00 and 21:00, respectively) at 23 ± 1 °C with free access to food and water. For in vivo delivery of Oct4-nanoscript, these particles were diluted with 0.9% saline and injected into the tail vein of five-month-old control and HGPS male mice. All mice were anesthetized with tribromoethanol (Avertin, 120 mg $k^{-1}g$) for the tail-vein injection. After injection, the mice were kept warm until full recovery from anesthesia. Two weeks after the first injection, the same mice were subject to the second injection of Oct4-nanoscript. Two weeks following this second injection, the mice were administered a third injection of the nanoscript to ensure sustained partial reprogramming. Seven weeks after the second injection, these mice were subjected to biochemical and histological analyses.

following treatment with Oct4-nanoscript or saline. Oct4-nanoscript treatment improves survival compared to the saline group. Saline-treated mice (Wild type $n = 9$; $LMNA^{G/G}$ $n = 8$) and Nanoscript-Oct4 treated mice (Wild type $n = 9$; $LMNA^{G/G}$ $n = 8$). ****$p < 0.0001$ according to log-rank(Mantel-Cox) test. F) The body weight percentages of $LMNA^{G/G}$ progeria mice and wild-type mice treated with Oct4-nanoscript or saline were measured weekly. Saline-treated mice (Wild type $n = 9$; $LMNA^{G/G}$ $n = 8$) and Nanoscript-Oct4 treated mice (Wild type $n = 9$; $LMNA^{G/G}$ $n = 8$). ****$p < 0.0001$ according to *two-way ANOVA* with Tukey's multiple comparisons test. G) Immunofluorescence staining of α-SMA (white) and DAPI (blue) in the aortic wall of $LMNA^{G/G}$ progeria mice and wild-type mice treated with Oct4-nanoscript or saline 2 months after treatment. Scale bar = 20 µm. H) Quantification of α-SMA-positive cells (top) and DAPI-positive cells (bottom) in the aortic wall of $LMNA^{G/G}$ progeria mice and wild-type mice. Data represent mean ± SEM. *One-way ANOVA-test*, *$P < 0.05$, **$P < 0.01$; $n = 6$ per group. I) Hematoxylin and eosin staining of liver, spleen, and kidney tissues from wild-type mice and $LMNA^{G/G}$ progeria mice treated with Oct4-nanoscript or saline 2 months after treatment. Scale bar = 50 µm. J) Quantification of hepatocyte density (left), area of germinal centers in the spleen (middle), and renal tubule diameter (right) in wild-type mice and $LMNA^{G/G}$ progeria mice. Data represent mean ± SEM. *One-way ANOVA-test*, *$P < 0.05$, **$P < 0.01$; $n = 3$ per group. K) Relative mRNA expression levels of *IL-6*, *Btg2*, and *Mmp13* in wild-type mice and $LMNA^{G/G}$ progeria mice treated with Oct4-nanoscript or saline. Data represent mean ± SEM. *One-way ANOVA-test*, *$P < 0.05$, **$P < 0.01$; $n = 3$ per group. L) Grip strength measurement of wild-type mice and $LMNA^{G/G}$ progeria mice treated with Oct4-nanoscript or saline. Data represent mean ± SEM. *Two-way ANOVA-test*, **$P < 0.01$; $n = 7$ per group.

Survival Rate and Body Weight Measurement: To assess the therapeutic effects of Oct4-nanoscript on lifespan extension and physical health, 4-month-old $LMNA^{G608G/G608G}$ progeria mice and wild-type littermates were randomly assigned to Oct4-nanoscript-treated or saline-treated groups. Mice received tail vein injections of Oct4-nanoscript or saline once weekly for 15 consecutive weeks. The dosage was consistent with the concentration used in prior in vivo experiments. Throughout the experimental period, all mice were monitored daily for general health status, activity levels, and appearance. For the survival analysis, $n = 8$ $LMNA^{G608G/G608G}$ progeria mice and $n = 9$ wild-type mice were included in each treatment group (Oct4-nanoscript-treated and saline-treated). Survival time was defined as the number of days from the start of treatment until natural death or euthanasia due to humane endpoints. Survival data were analyzed using the Kaplan-Meier method, and statistical significance was determined by the log-rank (Mantel-Cox) test. In parallel, body weight was measured weekly and recorded. Body weight changes were analyzed using the same animal cohorts ($n = 8$ $LMNA^{G608G/G608G}$ and $n = 9$ wild-type per group). Weekly body weight data were collected and statistically analyzed using two-way ANOVA followed by Tukey's multiple comparisons test to assess differences between treatment groups.

Open Field Test: The open field test was performed to assess locomotor activity and general mobility. Wild-type mice treated with Oct4-nanoscript or saline were placed in an open field chamber, and their movement was tracked for analysis. Total distance traveled and average velocity were measured using the EthoVision XT video tracking system. For distance measurements, $n = 5$ per group; for velocity measurements, $n = 6$ per group.

Grip Strength Test: Grip strength was measured using a grip strength meter (Jeungdo, JD-A-22) to evaluate muscle strength. Wild-type and $LMNA^{G608G/G608G}$ progeria mice treated with Oct4-nanoscript or saline were tested, and peak force was recorded. Each mouse was tested, and the maximum grip strength value was used for analysis. A total of $n = 7$ mice per group were used.

Mouse Fibroblast Culture: Tail-tip fibroblasts were isolated from 3-month-old $Lmna^{G608G/G608G}$ progeria mice. Following the previous protocol,[26] tail clips were excised using surgical scissors, immersed in 70% ethanol for 30 s three times, washed with 1× phosphate-buffered saline, and finely chopped with a sterile razor blade on a 10 cm tissue culture dish. The tissue fragments were then incubated with 0.25% trypsin for 30 min to aid in dissociation. The cells were cultured in mouse fibroblast medium (DMEM medium (Gibco) containing 10% fetal bovine serum (Gibco), 1% penicillin/streptomycin (Gibco), β-mercaptoethanol (Gibco), and non-essential amino acids (Gibco)) until reaching confluence. Subsequently, the cells were passaged once, pooled, and frozen for further use. For consistency, all experiments were conducted using cells between passages 4 and 6. Tail-tip fibroblasts were plated in a 12-well plate at a density of 5×10^5 cells per well. After 24 h, cells were incubated with various concentrations of Oct4-nanoscript for 8 h, followed by washing with a fresh mouse fibroblast medium. The culture medium was replaced every three days, and Oct4-nanoscript treated cells were maintained in an incubator at 37 °C with 5% CO_2.

Immunofluorescent Staining Analysis: Samples were washed with 1× phosphate-buffered saline and then fixed in 4% paraformaldehyde, followed by two washes with 1× phosphate-buffered saline containing 0.1% triton-X, based on a previously published protocol.[27] Primary antibodies were applied at the manufacturer's recommended dilution. The cells were incubated overnight at 4 °C with following primary antibodies: anti-Oct4 (Abcam, ab18976; Santacruz, sc-5279), anti-H3K9me3 (Abcam, ab8898), anti-H4K20me3 (Abcam, ab78517), anti-phospho-gamma H2AX (Cell signaling, 9718), anti-Lamin B (Santacruz, sc-374015), anti-Lamin A/C (BD Biosciences, 612 162), anti-p16INK4A (Invitrogen, PA5-20379), and anti-α-SMA (Invitrogen, 14-9760-82). The appropriate secondary antibodies were then applied for 2 h at room temperature. After two washes with 1× phosphate-buffered saline containing 0.1% Triton-X, the samples were treated with 6-diamidino-2-phenylindole (DAPI, Invitrogen) and mounted using Fluoromount-G mounting medium. Representative images were captured using a Zeiss confocal microscope (Zeiss, LSM800). All analyses were conducted by an investigator blinded to the experimental conditions. The number of nuclei in a field and the quantification of immunofluorescent signals within regions of interest were analyzed using Image J software. To ensure consistency, all data were processed in parallel using the same confocal microscope settings.

Western Blot Analysis: Following the previously published protocols,[28] cells and tissues were first washed twice with 1× phosphate-buffered saline before being lysed in RIPA buffer supplemented with a 1× proteinase inhibitor mixture to prevent protein degradation. To prepare the samples for electrophoresis, 5× SDS loading buffer was added, and the mixture was boiled for 5 min to denature the proteins. The lysates were then centrifuged at 12000 g for 10 min to remove any insoluble debris. Equal amounts of protein from the RIPA fractions were loaded onto a 12% sodium dodecyl sulfate-polyacrylamide gel (SDS-PAGE) and separated by electrophoresis. The proteins were subsequently transferred onto 0.2 µm nitrocellulose membranes. Primary antibodies were applied at the following concentrations and incubated with the membranes overnight at 4 °C: anti-Oct4 (1:500, Santacruz), anti-c-Myc (1:500, Cell Signaling), phospho-gamma H2AX (Cell Signaling), anti-H3K9me3 (1:1000, Abcam), anti-p16INK4A (1:1000, Invitrogen), anti-Histone H3 (1:1000, Cell Signaling), and β-actin (1:1000, AbFrontier). The next day, the membranes were washed and incubated with appropriate secondary antibodies conjugated to horseradish peroxidase (HRP) for signal detection. The chemiluminescent signals were detected using the ChemiDoc TRS+ system, and images were captured and analyzed using Image Lab software (Bio-Rad Laboratories).

Quantitative Real-Time Polymerase Chain Reaction Analysis: The detailed procedures were performed as previously described.[29] qRT-PCR analysis utilized 1/50 of the reverse transcription reaction and was conducted using a Rotor-Gene Q system (QIAGEN). Gene expression levels for each marker were normalized to GAPDH levels in the corresponding samples. The reaction conditions were optimized for each primer set to ensure efficient and specific amplification, typically involving an initial denaturation step, followed by a series of cycles consisting of denaturation, annealing, and extension phases. The specific gene primers used for this analysis were as follows: *Oct4* Forward: 5′-CTT CAG ACT TCG CCT TCT CA-3′ Reverse: 5′-GAT CCC CAA TAC CTC TGA GC-3′, *Sox2* Forward: 5′-GAA ACT TTT GTC CGA GAC CG-3′ Reverse: 5′- TCT TCA TGA GCG TCT TGG TT-3′, *Fgf4* Forward: 5′-GTG TGC CTT TCT TTA CCG AC-3′ Reverse: 5′-CAC TCG GTT CCC TTT CTG-3′, *Gdf3* Forward: 5′-GAC CTT TTG CAG TTT CTG GG-3′ Reverse: 5′-CAG CTC CTT CAC GTA GCA TA-3′, *Zfp42* Forward: 5′-AGG CCA AGG TGG AGC AAG-3′ Reverse: 5′-CCT GCA CCT GCT CAG ACA G-3′, *Utf1* Forward: 5′-GAA AAT GAC GAA CCT GCC C-3′ Reverse: 5′-GGG AGG ATT CGA AGG TAT GG-3′, *N-cadherin* Forward: 5′-GAC GGT TCG CCA TCC AGA C-3′ Reverse: 5′-TCG ATT GGT TTG ACC ACG G-3′, *Twist1* Forward: 5′-GTA CGA GGA GCT GCA GAC C-3′ Reverse: 5′-GGA AGT CGA TGT ACC TGG CC-3′, *Zeb2* Forward: 5′-GCA AAC AAG CCA ATC CCA GG-3′ Reverse: 5′-TTG CAG AAT CTC GCC ACT GT-3′, *E-cadherin* Forward: 5′-GGC ACA GAT GGT GTG ATT ACA GTC AAA A-3′ Reverse: 5′-GTC CCA GGC GTA GAC CAA A-3′, *Ssea1* Forward: 5′-GGA GGG AGC AGT GAC GCT AA-3′ Reverse: 5′-GGA GTA TGG GAG GGT GAT TC-3′, *Cldn3* Forward: 5′-TCA TCG GCA GCA GCA TCA TC-3′ Reverse: 5′-CCA GCA GCG AGT CGT ACA TT-3′.

Statistical Analysis: All data are presented as the mean ± SEM, obtained from three independent experiments. The value of n refers to either the number of independent experiments or the number of individual mice per experiment, with each experiment including three biological replicates. Statistical analyses were conducted using GraphPad Prism software. *P*-values were calculated using Student's *t*-test for two-group comparisons, and for multiple-group comparisons, one-way or two-way ANOVA was performed followed by Tukey's post hoc test, including the Tukey-Kramer test for pairwise comparisons. Two-way ANOVA with Tukey's multiple comparisons test were used for body weight progression and the Log-rank (Mantel-Cox) test were used for Percent survival. All of the statistical details of experiments can be found in the Figure legends.

Supporting Information

Supporting Information is available from the Wiley Online Library or from the author.

Acknowledgements

Ki-Bum Lee acknowledges the partial financial support from the New Jersey Commission on Spinal Cord (CSCR16ERG019; CSCR24IRG005), NIH R01 (1R01DC016612, 1R01NS130836-01A1, 3R01DC016612-01S1, and 5R01DC016612-02S1), NIH RM1 (RM1 NS133003-01), NIH R21 (R21 NS132556-01), and Alzheimer's Association (AARG-NTF-21-847862). This work was supported by the Basic Science Research Program through the National Research Foundation of Korea (NRF) funded by the Ministry of Education (NRF-2021M3E5E5096464 and RS-2023-00248303). This work was also supported by the ABC-based Regenerative BioTherapeutics (ABC project) grant funded by the Korean government (the Ministry of Science and ICT, the Ministry of Health & Welfare) (RS-2024-00433755).

Conflict of Interest

No. The authors declare no conflict of interest.

Author Contributions

H.K., J.K., and E.L. contributed equally to this work and are the first co-authors. H.K., J.K., and E.L. conducted most experiments. H.K., E.L., and B.C. performed, analyzed, and interpreted the nanoparticle characterization experiments. Y.H., H.K., and E.L. analyzed and interpreted the SPR experiments. J.K. designed and conducted the animal experiments. H.K., K.-B. L., and J.K. developed the key concept and designed the whole study. All authors contributed to the writing of this manuscript and have approved the final version.

Data Availability Statement

The data that support the findings of this study are available on request from the corresponding author. The data are not publicly available due to privacy or ethical restrictions.

Keywords

age-related diseases, artificial transcription factor, biomimetic nanoparticles, cellular rejuvenation, Oct4-nanoscript, partial reprogramming, progeria

Received: December 30, 2024
Revised: April 2, 2025
Published online:

[1] A. Parodi, N. Quattrocchi, A. L. van de Ven, C. Chiappini, M. Evangelopoulos, J. O. Martinez, B. S. Brown, S. Z. Khaled, I. K. Yazdi, M. V. Enzo, L. Isenhart, M. Ferrari, E. Tasciotti, *Nat. Nanotechnol.* **2013**, *8*, 61.

[2] a) H. Sun, J. Su, Q. Meng, Q. Yin, L. Chen, W. Gu, P. Zhang, Z. Zhang, H. Yu, S. Wang, Y. Li, **2016**, *28*, 9581; b) L. Chen, W. Hong, W. Ren, T. Xu, Z. Qian, Z. He, *Signal Transduction Targeted Ther.* **2021**, *6*, 225; c) H. Park, D. Kim, B. Cho, J. Byun, Y. S. Kim, Y. Ahn, J. Hur, Y. K. Oh, J. Kim, *Biomaterials* **2022**, *281*, 121327.

[3] a) X. Huang, Z. Cao, J. Qian, T. Ding, Y. Wu, H. Zhang, S. Zhong, X. Wang, X. Ren, W. Zhang, Y. Xu, G. Yao, X. Wang, X. Yang, L. Wen, Y. Zhang, *Nat. Nanotechnol.* **2024**, *19*, 545; b) H. Li, S. Zhou, M. Wu, R. Qu, X. Wang, W. Chen, Y. Jiang, X. Jiang, X. Zhen, *Adv. Mater.* **2023**, *35*, 2210920; c) H. Kim, B. Cho, H. K. Kim, S. Kang, S. An, D. Kwon, H. Y. Kim, J. Kim, *Nat. Commun.* **2025**, *16*, 2435.

[4] R. Hou, T. Lu, W. Gao, J. Shen, Z. Yu, D. Li, R. Zhang, Y. Zheng, X. Cai, *ACS Nano* **2022**, *16*, 9559.

[5] a) R. N. Mitra, R. Gao, M. Zheng, M. J. Wu, M. A. Voinov, A. I. Smirnov, T. I. Smirnova, K. Wang, S. Chavala, Z. Han, *ACS Nano* **2017**, *11*, 4669; b) Y. Liu, J. Du, M. Yan, M. Y. Lau, J. Hu, H. Han, O. O. Yang, S. Liang, W. Wei, H. Wang, J. Li, X. Zhu, L. Shi, W. Chen, C. Ji, Y. Lu, *Nat. Nanotechnol.* **2013**, *8*, 187.

[6] M. Alharbi, A. Lai, N. Godbole, D. Guanzon, S. Nair, F. Zuñiga, A. Quinn, M. Yang, S. Y. Wu, C. Salomon, *Int. J. Cancer* **2024**, *155*, 1510.

[7] H. Liu, L. Huang, M. Mao, J. Ding, G. Wu, W. Fan, T. Yang, M. Zhang, Y. Huang, H.-Y. Xie, **2020**, *30*, 2006515.

[8] a) S. Patel, D. Jung, P. T. Yin, P. Carlton, M. Yamamoto, T. Bando, H. Sugiyama, K. B. Lee, *ACS Nano* **2014**, *8*, 8959; b) K. Dardir, C. Rathnam, K. B. Lee, *Methods Mol. Biol.* **2017**, *1570*, 239.

[9] S. Patel, T. Pongkulapa, P. T. Yin, G. N. Pandian, C. Rathnam, T. Bando, T. Vaijayanthi, H. Sugiyama, K. B. Lee, *J. Am. Chem. Soc.* **2015**, *137*, 4598.

[10] S. Patel, P. T. Yin, H. Sugiyama, K. B. Lee, *ACS Nano* **2015**, *9*, 6909.

[11] S. Patel, S. T. Chueng, P. T. Yin, K. Dardir, Z. Song, N. Pasquale, K. Kwan, H. Sugiyama, K. B. Lee, *Angew. Chem.* **2015**, *54*, 11983.

[12] a) H. Kim, H. J. Park, H. Choi, Y. Chang, H. Park, J. Shin, J. Kim, C. J. Lengner, Y. K. Lee, J. Kim, *Stem Cell Rep.* **2019**, *12*, 518; b) S. Baek, X. Quan, S. Kim, C. Lengner, J. K. Park, J. Kim, *ACS Nano* **2014**, *8*, 10125; c) H. Kim, Y. J. Lee, Y. Kwon, J. Kim, *Sci. Rep.* **2023**, *13*, 21240.

[13] a) Q. Alle, E. Le Borgne, P. Bensadoun, C. Lemey, N. Béchir, M. Gabanou, F. Estermann, C. Bertrand-Gaday, L. Pessemesse, K. Toupet, R. Desprat, J. Vialaret, C. Hirtz, D. Noël, C. Jorgensen, F. Casas, O. Milhavet, J. M. Lemaitre, *Aging Cell* **2022**, *21*, 13714; b) A. Ocampo, P. Reddy, P. Martinez-Redondo, A. Platero-Luengo, F. Hatanaka, T. Hishida, M. Li, D. Lam, M. Kurita, E. Beyret, T. Araoka, E. Vazquez-Ferrer, D. Donoso, J. L. Roman, J. Xu, C. Rodriguez Esteban, G. Nuñez, E. Nuñez Delicado, J. M. Campistol, I. Guillen, P. Guillen, J. C. Izpisua Belmonte, *Cell* **2016**, *167*, 1719.

[14] a) R. Varga, M. Eriksson, M. R. Erdos, M. Olive, I. Harten, F. Kolodgie, B. C. Capell, J. Cheng, D. Faddah, S. Perkins, H. Avallone, H. San, X. Qu, S. Ganesh, L. B. Gordon, R. Virmani, T. N. Wight, E. G. Nabel, F. S. Collins, *Proc. Natl. Acad. Sci. USA* **2006**, *103*, 3250; b) K. C. Browder, P. Reddy, M. Yamamoto, A. Haghani, I. G. Guillen, S. Sahu, C. Wang, Y. Luque, J. Prieto, L. Shi, K. Shojima, T. Hishida, Z. Lai, Q. Li, F. K. Choudhury, W. R. Wong, Y. Liang, D. Sangaraju, W. Sandoval, C. R. Esteban, E. N. Delicado, P. G. Garcia, M. Pawlak, J. A. Vander Heiden, S. Horvath, H. Jasper, J. C. Izpisua Belmonte, *Nat. Aging* **2022**, *2*, 243.

[15] J. Kim, Y. Hwang, S. Kim, Y. Chang, Y. Kim, Y. Kwon, J. Kim, *Aging Cell* **2023**, *22*, 13825.

[16] C. Melander, R. Burnett, J. M. Gottesfeld, *J. Biotechnol.* **2004**, *112*, 195.

[17] H. Morinaga, T. Bando, T. Takagaki, M. Yamamoto, K. Hashiya, H. Sugiyama, *J. Am. Chem. Soc.* **2011**, *133*, 18924.

[18] G. J. Pan, Z. Y. Chang, H. R. SchÖLer, D. Pei, *Cell Res.* **2002**, *12*, 321.

[19] S. Narayan, G. Bryant, S. Shah, G. Berrozpe, M. Ptashne, *Cell Rep.* **2017**, *20*, 1585.

[20] P. Scaffidi, T. Misteli, *Science* **2006**, *312*, 1059.

[21] C. López-Otín, M. A. Blasco, L. Partridge, M. Serrano, G. Kroemer, *Cell* **2013**, *153*, 1194.

[22] A. Prieur, E. Besnard, A. Babled, J. M. Lemaitre, *Nat. Commun.* **2011**, *2*, 473.
[23] M. Ferreira-Marques, A. Carvalho, A. C. Franco, A. Leal, M. Botelho, S. Carmo-Silva, R. Águas, L. Cortes, V. Lucas, A. C. Real, C. López-Otín, X. Nissan, L. P. de Almeida, C. Cavadas, C. A. Aveleira, *Aging Cell* **2023**, *22*, 13983.
[24] S. Zhu, W. Li, H. Zhou, W. Wei, R. Ambasudhan, T. Lin, J. Kim, K. Zhang, S. Ding, *Cell Stem Cell* **2010**, *7*, 651.
[25] L. Han, G. N. Pandian, A. Chandran, S. Sato, J. Taniguchi, G. Kashiwazaki, Y. Sawatani, K. Hashiya, T. Bando, Y. Xu, X. Qian, H. Sugiyama, *Angew. Chem.* **2015**, *54*, 8700.
[26] a) J. Kim, S. C. Su, H. Wang, A. W. Cheng, J. P. Cassady, M. A. Lodato, C. J. Lengner, C. Y. Chung, M. M. Dawlaty, L. H. Tsai, R. Jaenisch, *Cell Stem Cell* **2011**, *9*, 413; b) B. Cho, J. Kim, S. Kim, S. An, Y. Hwang, Y. Kim, D. Kwon, J. Kim, *Adv. Sci.* **2024**, *11*, 2403105.
[27] a) H. Kim, S. Kim, B. Cho, J. Shin, J. Kim, *Transl Neurodegener* **2022**, *11*, 45; b) H. Kim, S. Kang, B. Cho, S. An, Y. Kim, J. Kim, *Adv. Sci.* **2025**, *12*, 2412548.
[28] a) H. Kim, B. Cho, H. Park, J. Kim, S. Kim, J. Shin, C. J. Lengner, K. J. Won, J. Kim, *Mol. Psychiatry* **2022**, *27*, 2751; b) H. Kim, J. Yoo, J. Shin, Y. Chang, J. Jung, D. G. Jo, J. Kim, W. Jang, C. J. Lengner, B. S. Kim, J. Kim, *Brain : a journal of neurology* **2017**, *140*, 2193; c) Y. Kim, H. Kim, B. Cho, S. An, S. Kang, S. Kim, J. Kim, *Front. Aging Neurosci.* **2024**, *16*, 1435445.
[29] a) H. Park, B. Cho, H. Kim, T. Saito, T. C. Saido, K. J. Won, J. Kim, *Nat. Commun.* **2023**, *14*, 802; b) H. Kim, S. Kim, S. J. Park, G. Park, H. Shin, M. S. Park, J. Kim, *Front. Aging Neurosci.* **2021**, *13*, 709091; c) H. Park, J. Shin, Y. Kim, T. Saito, T. C. Saido, J. Kim, *Transl. Neurodegener.* **2022**, *11*, 41.